Strained Interface Defects in Silicon Nanocrystals

Benjamin G. Lee, Daniel Hiller,* Jun-Wei Luo, Octavi E. Semonin, Matthew C. Beard, Margit Zacharias, and Paul Stradins*

The surface of silicon nanocrystals embedded in an oxide matrix can contain numerous interface defects. These defects strongly affect the nanocrystals' photoluminescence efficiency and optical absorption. Dangling-bond defects are nearly eliminated by H_2 passivation, thus decreasing absorption below the quantum-confined bandgap and enhancing PL efficiency by an order of magnitude. However, there remain numerous other defects seen in absorption by photothermal deflection spectroscopy; these defects cause non-radiative recombination that limits the PL efficiency to <15%. Using atomistic pseudopotential simulations, we attribute these defects to two specific types of distorted bonds: Si-Si and bridging Si-O-Si bonds between two Si atoms at the nanocrystal surface.

1. Introduction

Silicon has long dominated as a semiconductor material for the microelectronics and integrated circuit industries. However, until recently, its potential as an optoelectronic material has been limited, since bulk silicon is an indirect-gap semiconductor and hence a poor light emitter. This view was radically changed by the observation of strong room-temperature photoluminescence (PL) from quantum-confined Si.[1,2] Now, Si nanocrystals (NCs) are attracting significant attention as light-emitters, as well as for other optoelectronic applications that exploit quantum-confinement and the size-tunable bandgap. Potential uses range from light sources[3] such as LEDs and lasers, to Flash memories,[4] and all-silicon tandem solar cells, where the "top cell" consists of Si NCs.[5] Nonetheless, Si NCs pose significant challenges as a new material, in addition to the many anticipated opportunities. As a nanoscopic material with high surface-to-volume ratio, they can have numerous surface-interface defects. These defects could have deleterious effects for device applications.

Up to the present, the defects of Si NCs have been studied primarily with electron spin resonance (ESR),[6] or in terms of improved passivation leading to brighter PL.[7] ESR measurements are valuable for measuring and identifying different defect states that can be present in NCs; however, ESR is necessarily limited by the fact that it is only sensitive to paramagnetic defects. We are interested in all defects that can affect the desired optical and luminescent properties of the NCs. This motivates us to examine defects by sensitive measurements of optical absorption, which allow us to study transitions with low oscillator strength. We present a systematic study for samples of size-selected Si NCs, which have undergone different defect passivation treatments. This is complemented by atomistic pseudopotential theory simulations on realistic Si NCs to reveal the microscopic origin of the defects in the NCs and their properties, in agreement with the experiment.

Size-selected Si NCs embedded in SiO_2 are deposited by the superlattice (SL) approach on quartz glass substrates.[8] The NCs precipitate from the Si-rich SiO_x layers which segregate into Si and SiO_2 during high temperature annealing (1100 °C). Control over the NC diameter originates from the thickness of the SiO_x layer, which is confined between two stoichiometric SiO_2 layers. For this study three SL sample sets were prepared with SiO_x layer thicknesses of 2, 4, and 6 nm. The corresponding NC sizes, determined by TEM analysis, are approximately 2, 3.5, and 5.25 nm respectively.[9] In the rest of this paper, we will accordingly refer to the samples as 2, 3.5, and 5 nm NCs for simplicity (**Table 1**).

Recently, we have shown that the annealing ambient (N_2 or Ar) during the Si NC formation at 1100 °C has a substantial influence on the PL properties. Namely, for N_2 annealing nitrogen atoms get incorporated at the NC/SiO_2 interface and passivate some dangling bond defects.[9,10] About 50% less dangling-bond P_b-type defects and a doubled PL intensity were detected for N_2 annealed samples compared to inert Ar. Moreover, the capability of a post-annealing in H_2 ambient to passivate virtually all ESR active defects has been demonstrated.[6,11,12] In order to study the PL quantum efficiency (QE) and absorption properties not only as a function of NC size

---

Dr. B. G. Lee, Dr. P. Stradins
National Center for Photovoltaics
National Renewable Energy Laboratory
Golden, CO 80401, USA
E-mail: benjamin.lee@nrel.gov

Dr. D. Hiller, Prof. Dr. M. Zacharias
IMTEK - Faculty of Engineering
Albert-Ludwigs-University Freiburg
79110 Freiburg, Germany
E-mail: daniel.hiller@imtek.uni-freiburg.de

Dr. J.-W. Luo, O. E. Semonin, Dr. M. C. Beard
Chemical and Materials Science
National Renewable Energy Laboratory
Golden, CO 80401, USA

O. E. Semonin
Department of Physics
University of Colorado
Boulder, CO 80309, USA

DOI: 10.1002/adfm.201200572

Table 1. Overview of the Si NC superlattice samples investigated in this work.

Label	2 nm-Ar	2 nm-N_2	2 nm-N_2+H_2	3.5 nm-Ar	3.5 nm-N_2	3.5 nm-N_2+H_2	5 nm-Ar	5 nm-N_2	5 nm-N_2+H_2	5 nm-am
NC size	2 nm	2 nm	2 nm	3.5 nm	3.5 nm	3.5 nm	5.25 nm	5.25 nm	5.25 nm	5.25 nm
Main-annealing	Ar, 1100 °C	N_2, 1100 °C	N_2, 1100 °C	Ar, 1100 °C	N_2, 1100 °C	N_2, 1100 °C	Ar, 1100 °C	N_2, 1100 °C	N_2, 1100 °C	N_2, 850 °C
Post-annealing	–	–	H_2, 450 °C	–	–	H_2, 450 °C	–	–	H_2, 450 °C	–

but also their dependence on interface defect density the samples were annealed in three different ways (Table 1). A sample of each NC size was annealed at 1100 °C in Ar ambient, N_2 ambient, and N_2 ambient with subsequent H_2 post-annealing at 450 °C. One additional sample with amorphous nanoclusters was prepared by annealing at only 850 °C.[13]

2. Photoluminescence Spectra and Efficiency

Figure 1 shows a TEM cross-section of a typical Si NC sample. In this Z-contrast image (HAADF-STEM) the light grey color corresponds to Si NCs of ~3.5 nm in diameter. The superlattice structure as well as the separation of the NCs is clearly visible. Room temperature PL spectra with narrow spectral FWHM between 200–300 meV were measured corresponding to tight size distribution in each NC sample. Three example spectra (of NCs annealed in N_2 ambient and H_2 treatment) are shown in **Figure 2**a. As expected, the PL peak position shows a blueshift from 1.35 to 1.65 eV for decreasing NC size (Figure 2b). The PL peak position shows only a weak dependence on type of annealing treatment (small redshift by H_2 passivation[7] and small blueshift by incorporation of interfacial N[9]). The sample with amorphous Si nanoclusters showed extremely weak PL with a very broad peak.

The measured PL QE presented in Figure 2c shows a slight increase from Ar to N_2 annealing and up to an order of magnitude jump for H_2 passivation to ~13%. Previous PL measurements of Si NCs with different amounts of dangling bonds have only determined the relative PL intensities.[9,10] Here, we confirm the previously noted trend of increasing PL intensity for Ar < N_2 < N_2 + H_2 treated samples, and we establish

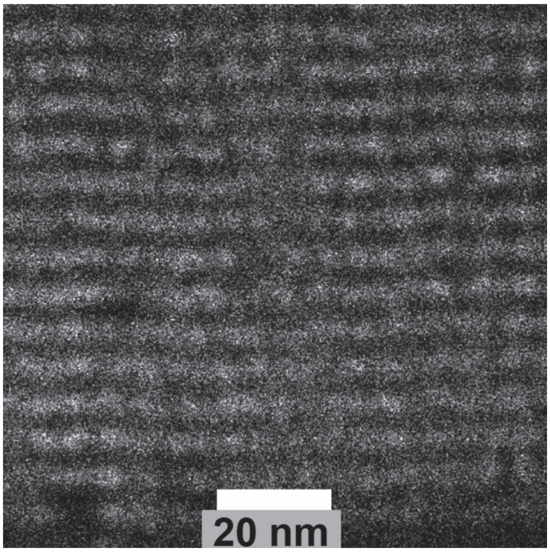

Figure 1. HAADF-STEM cross-section micrograph of NCs ~3.5 nm in diameter showing the crystallites and the superlattice structure.

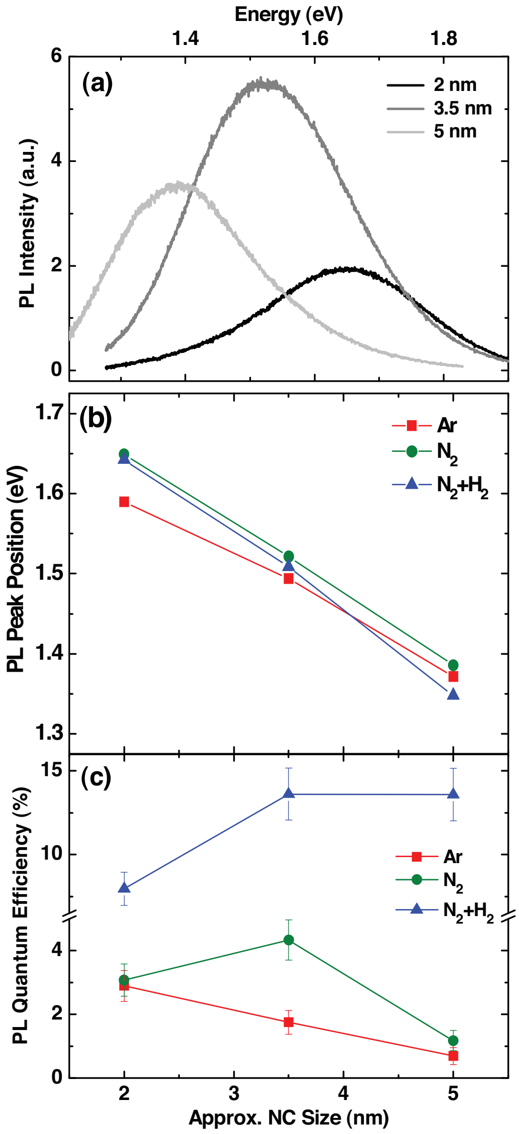

Figure 2. a) Sample PL spectra of the different-sized NCs. b) PL peak energies of size-selected NCs with different annealing treatments – Ar (red squares), N_2 (green circles), N_2 + H_2 (blue triangles). c) PL quantum efficiency of size-selected NCs with different annealing treatments.

an absolute measure of the PL quantum efficiency. We note that the amorphous sample exhibits QE of <0.1%, in agreement with Irrera et al.[14] who also found a very low QE for amorphous Si nanoclusters. We attribute this to the highly defective nature of amorphous Si nanoclusters.

PL QE is fundamentally equivalent to the ratio between the emission rate from radiative recombination, and all relaxation rates:

$$PL\,QE = \tau_{rad}^{-1} / \sum_i \tau_i^{-1} \tag{1}$$

Here we express PL QE in terms of the lifetimes for radiative and all relaxation processes τ_{rad} and τ_i respectively. Thus, PL QE of NCs can be limited by various different mechanisms that affect the rates of radiative vs. non-radiative recombination. In particular PL QE can be reduced by PL intermittency (blinking)[15,16] or by non-radiative recombination at defects.[17]

For PL intermittency, the OFF-switching of Si NCs has been demonstrated to be induced by Auger ionization.[15,16] This process requires excitation rates of $>10^4$ absorbed photons s^{-1} per NC to exceed the exciton decay time (~20 to 80 µs for our NCs[9]). If a second photon is absorbed by a NC that already has an exciton, the escape of a charge carrier from the NC to a trap state in its vicinity is enabled. Charged NCs cannot emit PL (OFF-state) because the additional electron-hole pair non-radiatively recombines via Auger processes and transfers its energy to excite the previously trapped charge carrier, resulting in reduced PL QE for the whole sample ($\tau_{Auger} \ll \tau_{rad}$). However, our measurements were done at low excitation intensity of only a few mW cm^{-2}, a flux of less than 10^3 s^{-1} per NC, making the Auger ionization mechanism and a significant contribution from PL intermittency unlikely. Instead, our results are consistent with PL QE being limited by recombination at defects.

Si NCs are known to have a particularly long radiative lifetime; for our NCs it is in the range of 20 to 80 µs.[9] Thus, the PL QE is vulnerable to even quite slow/weak non-radiative processes, which can be present due to electronic states associated with defects in the NC. We previously analyzed paramagnetic defects in Si NCs using electron spin resonance (ESR) (see Experimental Section and Figure S1).[9,11] These studies identified the one specific paramagnetic defect present – P_b-type dangling bonds, and associated them with the NC interface. The various different annealing treatments for NCs result in different defect densities. The defect density for NCs annealed at 1100 °C in Ar ambient corresponds to ~80% of them having a P_b defect, and ~60% of NCs annealed in N_2 ambient have a P_b defect. With annealing in N_2 ambient and a subsequent post-annealing in H_2 at 450 °C, only fewer than 2% of NCs have P_b defects.

Notably, the increasing trend in PL QE correlates strongly with annealing treatments that decrease defect densities. This is not surprising, since dangling bonds will clearly cause rapid non-radiative recombination in a NC. The PL QE increase from ~2% to 13% for the combined $N_2 + H_2$ treatment corresponds to a marked decrease in the non-radiative recombination rate τ^{-1}_{nr} from $\sim 50 \cdot \tau^{-1}_{rad}$ to $\sim 7 \cdot \tau^{-1}_{rad}$. However, a non-radiative rate seven times the radiative rate remains large! Therefore, it is clear that despite the effectiveness of the $N_2 + H_2$ treatment to almost eliminate paramagnetic defects, we still have significant non-radiative recombination. This implies the existence of other (non-paramagnetic) defects affecting recombination.

3. Defects and Near-Gap Optical Absorption

To gain a broader understanding of defects, including those that are not paramagnetic, we measure the near- and sub-bandgap optical absorption. To detect the low amount of absorption of the thin Si NC films near the bandedge, we employ a method sensitive to 10^{-4}–10^{-5} levels of absorbance – photothermal deflection spectroscopy (PDS).[18] The sample absorption data obtained by PDS was first corrected for the system response and then scaled to match the absolute sample absorption at 3 eV from spectrophotometer transmission/reflection measurements. PDS was also performed for bare quartz substrates that were treated by the same three annealing procedures as the NC samples. The absorption of the annealed, bare quartz was spectrally flat, featureless and at least an order of magnitude lower than that of our experimental Si NC film samples, even at the lowest photon energies. Another series of control samples was made with identical superlattice layers as the experimental samples, but not subjected to the high-temperature anneals that cause the segregation of excess Si into NCs. These suboxide superlattice control samples also had an order of magnitude lower absorption. This confirms that the observed absorption features are due to the Si NC superlattice stack, and specifically from the NCs rather than any remaining suboxide.[19] The initially measured data was divided by the thickness of the superlattice stack, thereby the absorption per cm of SL structure is obtained (**Figure 3**a–c).

The absorption shows several noticeable trends. First, all the curves display a "kink" corresponding to the transition between the tail of intrinsic bandgap absorption at higher energies and the flat defect absorption below gap. This kink occurs at higher energies for smaller NCs, as expected from quantum confinement. Moreover, within each sample set having the same NC size but different annealing treatments, all the curves have this kink at similar photon energy. This agrees with the PL peak data, which is also consistent with the bandgaps being set by NC size, and only weakly modified by the annealing treatments. The amorphous nanoparticles of the 850 °C annealed 5 nm size sample (Figure 3c) exhibit substantially higher absorption that we attribute to the amorphous and highly defective nature of the sample; note that there is no kink visible corresponding to a transition between defect states and intrinsic bandgap absorption.

The second observation is that the near- and sub-gap absorption for each size-selected sample set is: a) nearly the same for the 3 different annealing treatments, but b) does show a trend where absorption is highest for the Ar treatment, then the N_2 anneal, and lowest for the $N_2 + H_2$ passivation. Notably, the "kink" at the bandgap becomes more pronounced for the latter annealing treatments. The trend in absorption Ar > N_2 > $N_2 + H_2$ implies successively decreasing defect density, in agreement with the ESR results. However, all 3 annealing treatments still show substantial below-gap absorption. Indeed, the below-gap

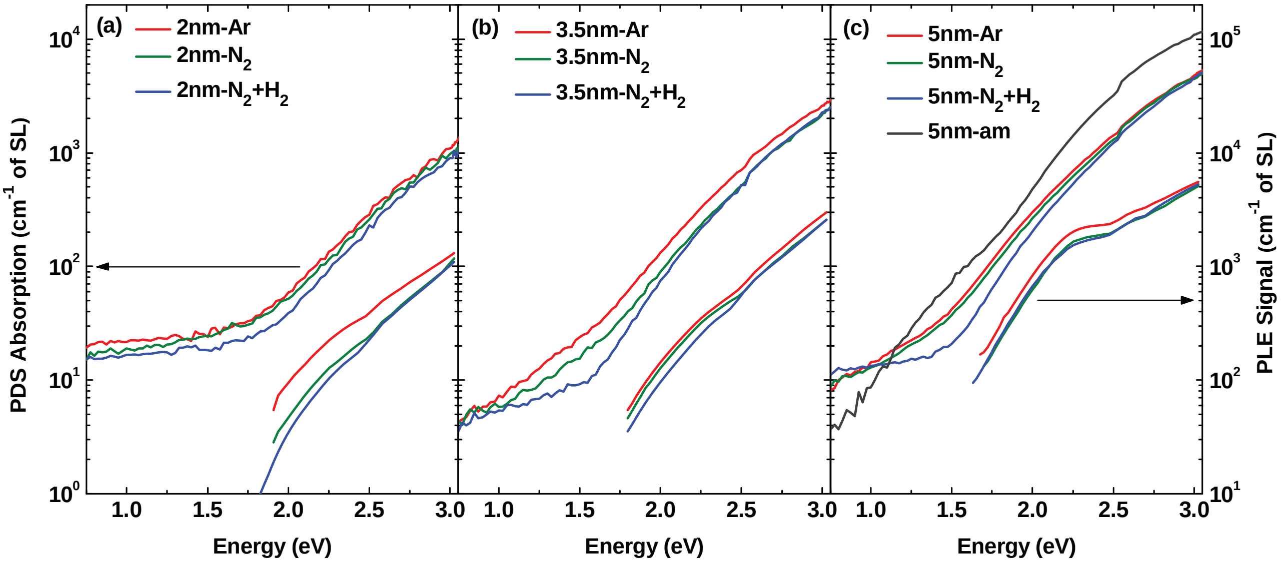

Figure 3. PDS absorption and PLE for size-selected NCs with different annealing treatments – Ar (red), N_2 (green), $N_2 + H_2$ (blue), amorphous nanoclusters (black), a) 2-nm, b) 3.5-nm, and c) 5-nm NCs. PLE data is offset by 1 decade for clarity.

absorption is only slightly lower for $N_2 + H_2$ treated samples than for the unpassivated samples. This means that even when virtually all P_b defects are passivated (with $N_2 + H_2$ treatment), there remain numerous other defect states that are not passivated and contribute to the absorption. Importantly, these residual non-paramagnetic defects are likely responsible for limiting the observed PL QE to <15%. The relatively low QE values point to non-radiative processes rapid enough to compete with luminescence, for basically all NCs. Thus, practically all NCs have remaining defects that prevent us from reaching the expected near-unity QE for truly defect-free NCs, where only radiative recombination is present.

With PDS, we measure the non-radiative fraction of absorption in each sample, since this is responsible for the thermal signal. This includes: (1) below-gap absorption by defects in the Si NCs; (2) non-radiative recombination of photocarriers generated by above-gap absorption in NCs; (3) thermalization of hot photocarriers to the band-edge in NCs. To gain a deeper understanding of the role of the defects, it is useful to independently measure the fraction of absorption which is re-radiated as PL. This is possible with photoluminescence excitation (PLE) measurements, which in contrast to PDS is only sensitive to absorption that is re-emitted. The PLE response of the samples is monitored at the emission peak of each sample (peak energies of Figure 2b) and then normalized to the absorption of the Si NC samples at 3 eV. In Figure 3 the PLE data is plotted on the same logarithmic axes as the PDS data but offset by 1 decade for clarity.

PLE results are substantially similar to the absorption determined by PDS, particularly at higher energies. However, close to the bandedge, the data diverge from the PDS results. Near the bandedge, the PDS data displays an exponential tail of absorption that flattens into the below-gap defect absorption. In contrast, the PLE data shows a faster than exponential decrease in approaching the bandedge. Moreover, this trend is seen in all the samples (Ar, N_2 and $N_2 + H_2$). This is markedly different than in the PDS data where the Ar and sometimes the N_2 treated samples display a much more shallow drop near the bandedge, as opposed to the steeper decline of $N_2 + H_2$ treated samples. In particular, the PLE data for 2-nm NCs (Figure 3a) shows a declining absorption even below 2 eV, where the PDS absorption has already flattened out due to defect absorption. 5-nm NCs (Figure 3c) have an unexplained "bump" in the PLE data near 2.2 eV, but aside from that anomaly, the results follow the trends outlined above. Thus, the crucial difference between the PDS and PLE data is the lower absorption from near- and sub-gap states seen for PLE.

From this, we deduce that the near-gap absorption features seen by PDS cannot be simply due to the intrinsic absorption of multiple different energy gaps (from the size-distribution of the NCs). Clearly, this effect would be seen in the PLE data as well. Therefore, since these states are observed by PDS but not PLE, we conclude that they must be defect states that absorb light but do not contribute to PL. Thus, in order to achieve a higher PL QE or a less-defective material for applications, it is necessary to understand and inactivate these defects. We continue in the following sections with an analysis of the absorption edge and theoretical studies to further our understanding of the defects.

4. Analysis of Absorption Edge

We examine in more depth the absorption edge of the PDS data (Figure 3), which shows an exponential dependence. This is an expected feature of a defective material, in contrast to defect-free semiconductors whose above-gap absorption follow the relationship for either direct or indirect band-to-band transitions.[20]

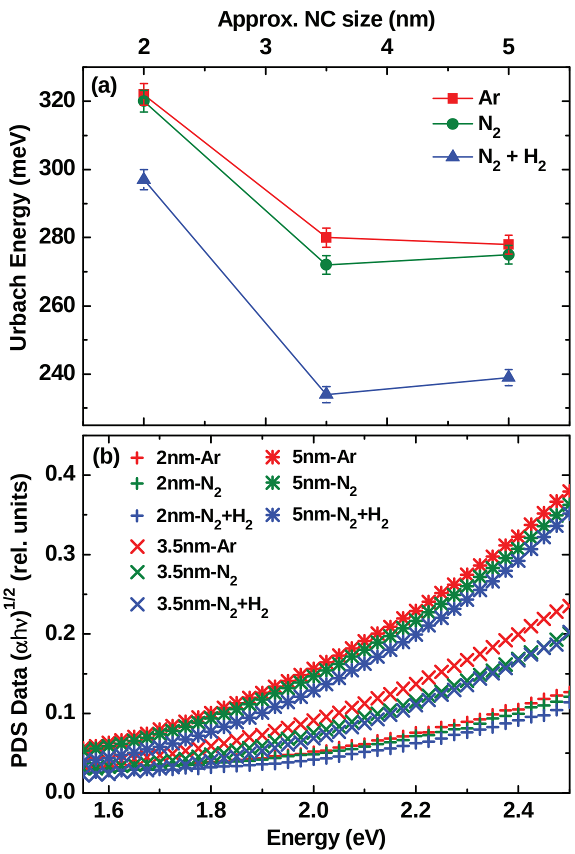

Figure 4. a) Urbach energies from PDS for size-selected NCs with different annealing treatments – Ar (red squares), N_2 (green circles), N_2 + H_2 (blue triangles). b) Tauc plot using absorption determined by PDS of NCs with different annealing treatments–Ar (red), N_2 (green), N_2 + H_2 (blue) of 2-nm (+), 3.5-nm (×), 5-nm NCs (*).

The exponential dependence found here is characterized by the empirical expression:

$$\alpha = \alpha_0 \exp\left((E - E_0)/E_U\right) \tag{2}$$

where α_0 and E_0 are characteristic parameters of the material and E_U is the Urbach energy.[21] The Urbach energy describes the width of the absorption edge, so that a small E_U corresponds to a steep rise in absorption. Absorption by bandedge defect states will make the absorption edge shallower, corresponding to larger E_U. By fitting the exponential dependence of the absorption edge in the PDS data, we quantify E_U for each of the samples (**Figure 4**a).

We find that the Urbach energies are in the range ~200–300 meV, which is in the range of previously reported E_U values for Si NCs.[22–25] In addition, the increase of E_U with decreasing NC size can be confirmed here.[22,23] We attribute this size trend to the greater surface-to-volume ratio of smaller NCs, leading to an increased effect of the NC/SiO_2 interface states. Our results also show a clear trend of decreasing E_U for increasing P_b defect passivation. The $N_2 + H_2$ treatment, which provides the best passivation, clearly has the smallest E_U out of each size-selected sample set. This reinforces the link between annealing treatments and P_b defect passivation that we already noted in the PDS data.

The exponential tail observed in the PDS data masks the absorption signature of band-to-band transitions that we might expect to see from the Si NCs, as we have just noted in the Urbach energy analysis. While strictly speaking, quantum-confined NCs do not necessarily follow the Tauc rule for bulk indirect (or direct) semiconductors,[26] empirically it is still useful to make a Tauc plot of their absorption. In Figure 4b we show the PDS absorption displayed according to the linear $(\alpha h\nu)^{1/2}$ vs. $h\nu$ Tauc dependence expected for (bulk) indirect semiconductors.[20] All the curves diverge widely from linearity, especially at lower energies closer to the gap. This trend holds even for the less defective $N_2 + H_2$ annealed samples. (We note that the PDS absorption does not follow the relation for direct semiconductors either.) This is perhaps additional evidence that even the $N_2 + H_2$ annealed samples have a significant residual defect density, which is responsible for the bandtail absorption that deviates from the Tauc rule. Alternatively, it may be that the Tauc relationship is not valid for Si NCs.

Since the PLE measurements exclude sub- and near-gap defect absorption (because it does not contribute to PL), we expect a better fit for the PLE data to the Tauc relationship. This is in fact the case, shown here in the Tauc plot of PLE data (**Figure 5**a). Indeed, the fit of data to the Tauc rule for indirect

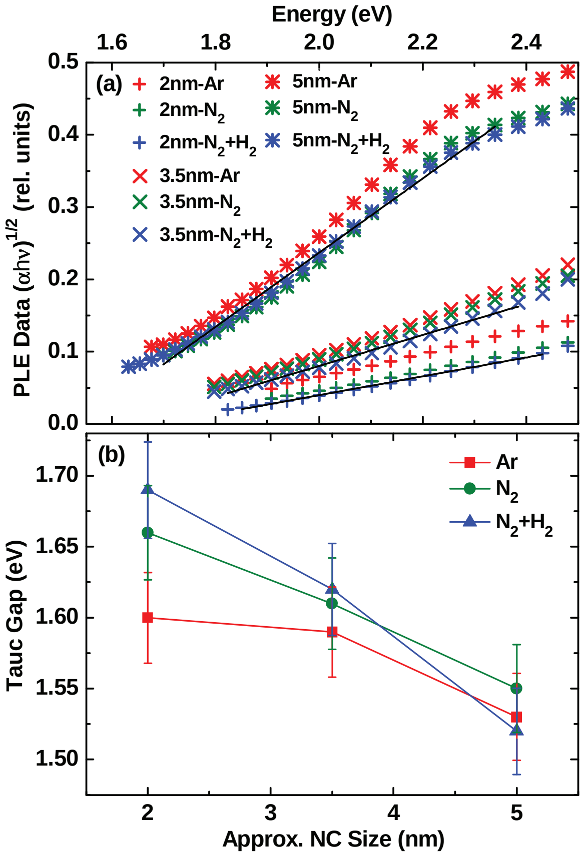

Figure 5. a) Tauc plot using PLE data of NCs with different annealing treatments – Ar (red), N_2 (green), $N_2 + H_2$ (blue) of 2-nm (+), 3.5-nm (×), 5-nm NCs (*). Linear fits for $N_2 + H_2$ data shown as solid lines. b) Tauc gaps of size-selected NCs with different annealing treatments.

semiconductors is quite good, regardless of the samples' annealing treatment. Importantly, the relationship holds for the entire range from just above the bandedge to ~2.5 eV, which is the same range in which bulk crystalline Si obeys the Tauc rule. Moreover, the fact that the Si NCs have some size distribution does not seem to cause a deviation from the Tauc rule, perhaps because the distribution is narrow.

Extrapolating, we obtained the Tauc gap energies presented in Figure 5b. We note that the trend of the Tauc gaps behaves as expected with the NC size. The Tauc gaps roughly mirror the PL peak energies (Figure 2b), though they are blue-shifted by ~ 20 to 160 meV. The uncertainty in the Tauc gap values obtained from our analysis prevent us from making any firm conclusions on the magnitude of this energy difference which is often referred to as a Stokes shift, but it appears consistent with previous experimental findings.[27] However, according to Kovalev et al. the interpretation of the observed energy shift as a Stokes shift is misleading and it is more likely to have its origin in the very small density of states that exists near the exciton ground state.[28] If the Si NCs were actually direct-gap, their size distribution could make the absorption resemble an indirect-like Tauc behavior in the near-gap region. However, the apparent Tauc gap values would be red-shifted from the PL peak energies, because of strong absorption from the larger NCs with smaller energy gaps. This is not seen in our measurements.

According to the Tauc plot, Si NCs down to 2 nm in size have intrinsic bandgap absorption (i.e. when defect absorption is subtracted or not present) characteristic of an indirect-gap semiconductor. This finding of indirect-gap Tauc behavior for size-selected Si NCs reinforces which was first suggested by PLE measurements of NCs created with ion-implantation.[27] This has also been claimed from absorption measurements.[29–32] However, in previous absorption measurements the linear $(\alpha h\nu)^{1/2}$ vs. $h\nu$ relationship holds only for a narrow range of energies (not both near-bandedge as well as higher energies), due to defect absorption affecting the bandedge, which we also noted for our PDS absorption data. We would argue that this non-negligible defect absorption masks the intrinsic absorption near the bandedge, resulting in potentially inaccurate assignments of Tauc gaps. An accurate determination of the Tauc gap can only be achieved with a well-passivated, nearly defect-free NC sample, or by using a technique such as PLE that is insensitive to defect absorption.

5. Nature of Defects

We now examine the possible origin and nature of the defects responsible for the sub-gap optical absorption and non-unity PL QE seen in the Si NCs. These are the non-paramagnetic defects that persist after H_2 passivation of the NCs, when basically all the dangling-bond defects have been inactivated. We assert that the defects are associated with the interface between the NCs and the surrounding oxide, rather than being internal to the NCs or outside in the oxide matrix. A defect in the interior of the NC, such as a vacancy or interstitial in the Si lattice, is extremely unfavorable energetically. A substitution with an impurity atom is possible, but previous elemental analyses (ToF-SIMS, RBS, ERDA) rule out impurities as a factor.[9] As for defects in the oxide, if these defects are not very close to the interface, they would have negligible influence on the optical properties of the NCs, particularly the PL QE. Significant overlap of the defects with the electron density in the NCs is required.

The dangling-bond P_b-type defects that were identified using ESR are one type of interface defect seen in the NCs. However, these were almost entirely inactivated by H_2 passivation treatments. What other types of interface defects might remain, which are non-paramagnetic? One possibility is dangling bonds that are charged and hence not detectable by conventional ESR. We investigated this by doing ESR with illumination (LESR), where charged defects may be detected. However, no additional defect signals were detected with H_2 passivated samples. Thus we believe that charged dangling-bonds are also negligible or absent after passivation.

Theoretical calculations have revealed that other types of interface defects are possible in silica-embedded Si NCs besides P_b centers.[33] Specifically, distorted Si-Si bonds and Si-O-Si bridging bonds – these are bonds connecting 2 Si atoms belonging to the NC and located at its surface (interface). In this work, we have performed calculations using an atomistic pseudopotential method to describe the electronic structure of Si NCs embedded in amorphous SiO_2. The atomic configuration is generated by starting with a cubic supercell of SiO_2 β-crystobalite structure, closest to the diamond structure among the SiO_2 polymorphs, containing about 8200 atoms and then removing all O atoms within a predetermined radius from the center of the cell to mimic the Si NC.[33] Following the relaxation of the atomic position to minimize the strain energy, the amorphous state of SiO_2 is generated using the Monte Carlo algorithm of Wooten, Winer, and Weaire.[34] The strain energy is described with a valence-force-field-type Hamiltonian under an assumption of defect-free configuration, in which Si and O have four and two bonds, respectively, and there are no O-O bonds.[35]

In the fully relaxed atomic configurations of Si NCs embedded in amorphous SiO_2, a considerable number of Si-O-Si bridge bonds and large distortions of Si-Si bonds were found at the surface of the NCs. These are considered as two sources of the defect states inside the bandgap of Si NCs.[33,36] Here we investigate the contributions of these two sources to the defect states by explicitly calculating the electronic structure of these Si NCs using our atomistic pseudoptential method. The electron states of Si NCs are obtained from solving the Schrodinger equation,[37]

$$\left[-\frac{\hbar^2}{2m}\nabla^2 + V\left(\vec{r}\right)\right]\psi_i\left(\vec{r}\right) = \varepsilon_i\psi_i\left(\vec{r}\right) \tag{3}$$

where $\{\varepsilon_i, \psi_i\}$ are energy and wavefunction of state i, m is the bare electron mass, and is the Planck constant. The crystal potential $V\left(\vec{r}\right)$ is a superposition of screened atomic potentials $\hat{\upsilon}_\alpha$ of atom type α located at atomic site $\vec{R}_n$ within the primitive unit cell n:[38–40]

$$V\left(\vec{r}\right) = \sum_{n,\alpha}\hat{\upsilon}_\alpha\left(\vec{r} - \vec{R}_{n,\alpha}\right) \tag{4}$$

thus forcing upon us the correct atomically resolved symmetry. The construction of the screened atomic potentials $\hat{\upsilon}_\alpha$ is the key

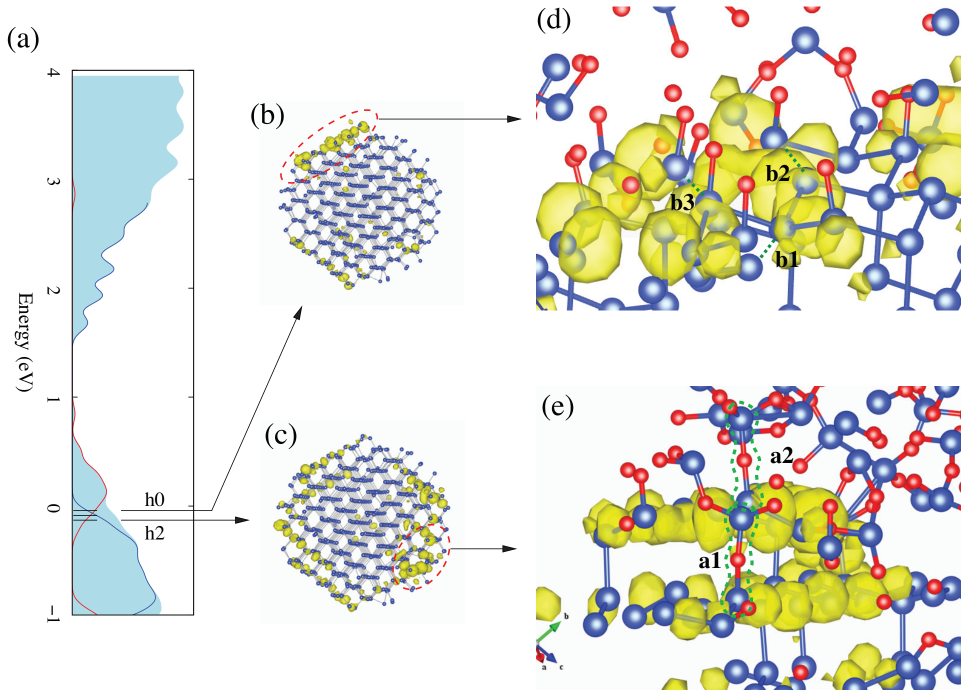

Figure 6. a) Density of states calculated from theory for a 3 nm diameter Si NC. Blue and red lines respectively denote states where the wavefunction probability density is primarily in the interior of the NC vs. states primarily on the surface of the NC. b) and c) Hole states of the Si NC in the valence-band, where the wavefunction probability density is primarily near the surface of the NC. Surrounding oxide matrix has been removed for clarity. d) Distorted Si-Si bonds present near the surface of the NC. Three such bonds (b1, b2, b3) are marked with dashed green lines. e) Distorted Si-O-Si bridge bonds (a1 and a2, contoured by dashed green line) present near the surface of the NC.

to accuracy and realism. To remove the "LDA error" of bandgap and effective masses in the bulk crystal, $\hat{v}_{\alpha}$ was fitted to reproduce well not only the experimental band gaps throughout the zone, but also the electron and hole effective-mass tensors, the spin-orbit splittings, and the hydrostatic and biaxial deformation potentials of bulk Si and SiO_2, as well as the valence band and conduction band offsets between Si and SiO_2. The computation capacity of our atomistic pseudopotential method is aggressively extended from <1000 atoms of LDA (and <100 of atoms using the GW and Bethe-Salpeter method) to up to millions of atoms with the present method.[40]

Figure 6 shows the electronic structure results of a relatively large NC with diameter of 3 nm (Si NC containing 801 Si atoms and SiO_2 matrix has 6015 atoms). The density of states (DOS) shown in Figure 6a is qualitatively divided into two parts – intrinsic NC quantum confinement states (mostly confined inside the NC) presented by the blue line and surface defect states (mostly localized on the surface) presented by the red line, by checking the spatial charge density distribution of each state. Two typical defect states near the highest-occupied-molecular-orbital (HOMO), associated with distorted Si-Si bonds and Si-O-Si bridge bonds respectively, are shown in Figure 6b-c along with the atomic structure of the Si NC (oxide is removed for visualization).

Interestingly, these two defect states are somewhat delocalized over the NC surface, rather than well localized around a certain defect as we expected.[36] This delocalization feature of defect states is because of the high defect density on the Si NC surface and interaction between different defects. The correlation between wavefunction distribution and atomic structure of defects is given in Figure 6d-e. In Figure 6d we find that the defect state labeled "h0" is associated with distorted Si-Si bonds with long lengths, b1 = 4.33, b2 = 3.49, and b3 = 3.65 Å in comparison to the equilibrium Si-Si bond length of 2.35 Å. The "h2" defect state in Figure 6e is associated with distorted Si-O-Si bridge bonds. The bond lengths and angles of bridge bonds a1 and a2 are respectively (1.590 Å, 1.586 Å, 169 degrees) and (1.608 Å, 1.616 Å, 163 degrees); this deviates from the normal value of (1.60 Å, 1.60 Å, 145 degrees). Therefore our atomistic calculation confirms the previous suggestion that Si-O-Si bridge bonds and large distortions of Si-Si bonds at the silica-embedded Si NC surface are two important sources of defect states and that they reduce the bandgap of Si NCs.[33]

Importantly, the existence of these strained interface defects does not require that the bulk of the Si NC be strained. In the calculation, the bond lengths in the interior of the NC are all close to the equilibrium Si-Si bond length. Nonetheless, there is some experimental evidence of overall strain in the NCs. Raman measurements show a peak-shift of the Si TO-phonon mode that competes with the effects of phonon confinement. Models attribute this shift to several GPa of compressive strain that increases with decreasing NC size.[41,42] Additionally, the fact that ESR measurements showed P_{b1} dangling-bond defects in our samples strongly supports the idea of strained Si–Si bonds at the Si NC/SiO_2 interface. This is because the P_{b1} defect is an interfacial strained $Si_3{\equiv}Si\bullet$ dimer (here the dot represents the unpaired electron) as shown in Figure S1.[43]

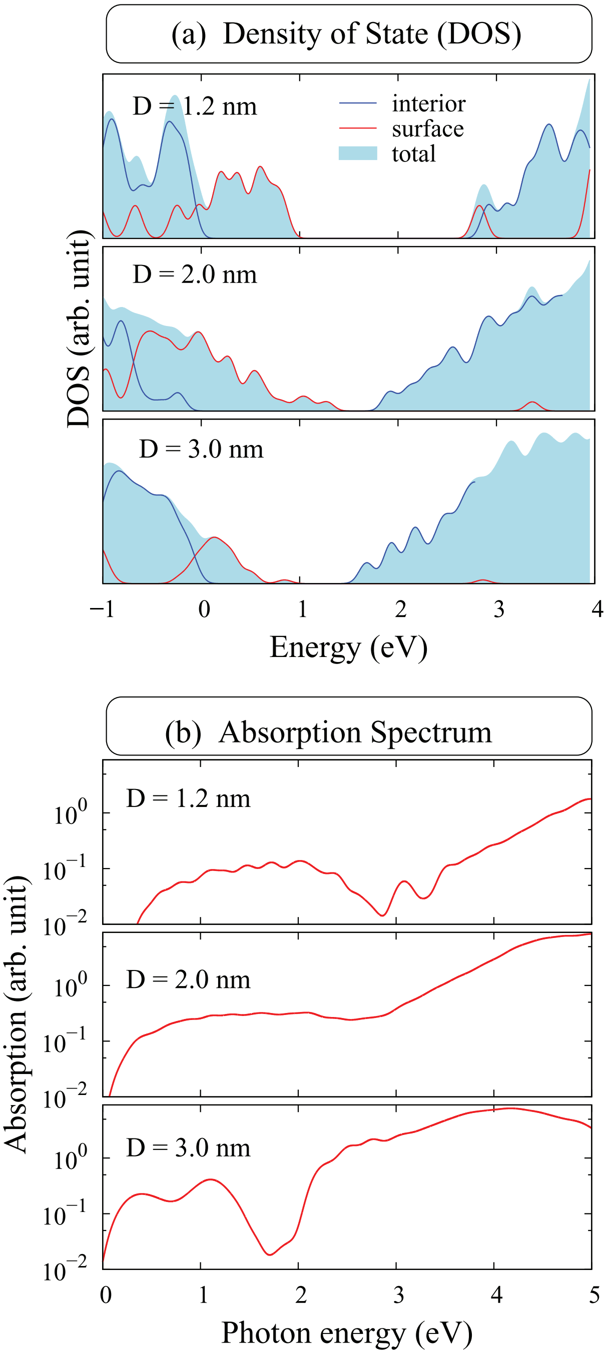

Figure 7. a) Density of states calculated from theory for different sized Si NCs. Blue and red lines respectively denote states where the wavefunction probability density is primarily in the interior of the NC vs. states primarily on the surface of the NC. b) Corresponding absorption spectra plotted on a log scale. Calculation does not include the effect of phonons on the optical absorption.

Recall that for the Si NCs, we experimentally observed optical absorption in the near- and sub-bandgap regions. To compare our theory to the experiment, we calculate the contribution of the two types of defect states to the optical absorption. In **Figure 7**, we present our atomistic method calculated absorption spectra as well as DOS of Si NCs with diameters of 1.2, 2.0, and 3.0 nm. Indeed, we find relatively strong optical transitions in the near-gap region between defect states, which are much stronger than that of intrinsic band-edge $\Gamma - X$ transition. Calculated below-gap absorption is also considerable, in agreement with experimental PDS measurements in Figure 3. The observed strongest above-gap absorption peak in Figure 7b arises from the $\Gamma - \Gamma$ transitions of intrinsic quantum confined states. Thus, our theory results can explain the near- and sub-gap optical absorption seen in the experiments.

Defect states are not usually involved with luminescent optical transitions, and instead act as non-radiative recombination centers. Therefore, our theory can additionally explain the non-unity PL QE seen in the Si NCs despite the apparently complete passivation of P_b center defects. Namely, the PL QE still remains reduced by non-radiative recombination at relatively numerous residual non-paramagnetic defects such as distorted Si-Si bonds and Si-O-Si bridge bonds. We expect that basically all NCs will have these defects, which explains the relatively low PL QE observed.

6. Conclusions

We observed a nearly order of magnitude improvement in PL quantum efficiency to 13% in size-selected Si NCs embedded in silica, by annealing treatments with reactive gases (N_2 and H_2). We attributed the increased PL to the passivation of defects. Defect passivation was clearly indicated by the decreased defect absorption in the exponential tail at the band-edge, which was seen in PDS measurements. This near-band-edge absorption follows the Urbach rule; decreasing Urbach energies were associated with decreased defect density. However, our measurements also revealed a considerable amount of non-paramagnetic near- and sub-gap defect states that remain after passivation, and which drastically limit the PL quantum yield. Indeed, the QE values of <15% mean that non-radiative recombination processes compete with PL in nearly all NCs, due to ubiquitous defects. Our theoretical calculations indicate that the origin of these defects are distorted Si-Si bonds and Si-O-Si bridging bonds at the NC/SiO_2 interface. Beyond silicon, strained surface interfaces may play a major role in numerous other nanocrystalline materials.

7. Experimental Section

Sample Preparation: Si NCs embedded in a SiO_2 matrix are grown by a two-step process. First, 50 SiO_2/SiO_x bilayer stacks were deposited on quartz glass (GE-214) substrates by reactive thermal evaporation of SiO powder under an O_2 pressure (8×10^{-4} mbar) or high vacuum, respectively.[8] The stoichiometry of the SiO_x is $x = 1.2$, previously confirmed by Rutherford backscattering (RBS) measurements. Each sample set has a different SiO_x layer thickness: 2, 4, and 6 nm, which approximately determines the NC size.[9] SiO_2 spacing layer thicknesses are always 3 nm; the capping SiO_2 is 10 nm thick. Next, Si NCs form in the SiO_x layers during annealing in a quartz tube furnace (1100 °C, 1 h) in high purity inert gases (Ar or N_2) which avoids significant loss of NC layers due to oxidation.[9] For each size-selected NC sample set, one piece is annealed in Ar, a second in N_2, and a third also in N_2 followed by a treatment in pure H_2 for 1 h at 450 °C. One additional sample with

6-nm thick SiO_x layer is annealed in N_2 for 1 h at only 850 °C to induce the formation of amorphous Si nanoclusters.[13] High angle annular dark field (HAADF) cross-section images in scanning TEM mode were obtained with an FEI TITAN 80-300.

PL and QE Measurements: PL spectra were obtained with a LN_2-cooled CCD attached to a single grating monochromator under excitation of a HeCd laser (3.8 eV). All spectra were corrected for the spectral response of the setup. The absolute PL QE η_{PL} is measured in a LabSphere integrating sphere, with excitation of 420 nm (selected from a xenon lamp passed through a monochromator). The excitation and emission spectra are fiber coupled to an LN_2-cooled silicon CCD spectrometer. All spectra are corrected for grating, fiber, sphere, and detector efficiencies using a calibrated lamp. Determination of the η_{PL} consists of integrating four spectral scans of the sample and of a reference (bare quartz) substrate:[44]

$$\eta_{PL} = \frac{\int I_{sample}(\lambda) - I_{ref}(\lambda)\, d\lambda}{\int E_{ref}(\lambda) - E_{sample}(\lambda)\, d\lambda} \tag{5}$$

where E_{ref} is the photon flux of the excitation light measured with the bare substrate, E_{sample} is the flux of the transmitted and reflected excitation light with the NC sample, and I_{sample} is the flux of the emitted light. The denominator and the numerator represent the photon flux absorbed and emitted by the film, respectively. Background effects (such as the tail of the excitation) are removed by subtracting the background emission spectrum, I_{ref}.

Absorption Measurements: For photothermal deflection spectroscopy (PDS) [18] samples were placed in a quartz cuvette containing a perfluorocarbon liquid (3M Fluorinert FC-77). The sample was illuminated with a pump beam of monochromatic light oriented perpendicular to the sample surface; the pump source consists of a tungsten filament lamp, chopped at 9.88 Hz and passed through a monochromator and reflective focusing optics. A fraction of the pump beam is absorbed in the sample, heating it and causing a thermal and refractive-index gradient in the liquid near the sample's surface. Similar to a desert mirage, the gradient in refractive index deflects a probe beam (HeNe laser); the deflection is detected by a split-diode and lock-in amplifier. System response, including effects of source brightness and grating efficiencies, was determined using an amorphous carbon film deposited on the same type of quartz substrate. This film has a nearly flat absorption spectrum for photon energies from 0.5 to 3 eV, which was determined from transmission and reflection spectra from a Cary 6000i UV-Vis spectrophotometer. PLE measurements used variable-wavelength excitation from a xenon lamp passed through a monochromator, with slit-width fixed for 10-nm excitation bandwidth. The excitation intensity is monitored by a calibrated silicon diode and the emission spectra are fiber-coupled to an LN_2-cooled silicon CCD spectrometer. Emission spectra are corrected for system response using a calibrated lamp.

Electron Spin Resonance (ESR): Figure S1 shows first derivative K-band (20.45 GHz) ESR spectra of Si NC superlattice samples with identical size but different annealing treatments measured at 4.2 K. All spectra are corrected for position, sample area, and Si:P marker intensity (for N_2+H_2 treated samples, a weaker marker was used, to allow comparison with the low signal intensity). Two major point defect centers can be identified: EX (SiO_2 specific and without influence on the NCs) and P_b-type (dangling bonds at the Si NC/SiO_2 interface). The dangling bond signal decreases significantly when N_2 instead of Ar is used as the ambient during annealing at 1100 °C, and the H_2 post-annealing is shown to eliminate almost all P_b-type defects. The decomposition of the P_b-type signal into its components $P_{b(0)}$ and P_{b1} (which involves a strained Si–Si bond) is explained in Ref. [11]. A schematic of the P_{b1} defect is shown in Figure S1 inset.

Supporting Information

Supporting Information is available from the Wiley Online Library or from the author.

Acknowledgements

Both corresponding authors contributed equally to this work. We thank E. Pippel (MPI Halle) for HAADF-STEM, K. Riskey and C. Taylor (Colorado School of Mines) for LESR, A. Zunger (CU Boulder), H. Branz (NREL), A. Stesmans and M. Jivanescu (KU Leuven) for discussions. J.W.L. thanks G. Hadjisavvas for generating the atomic structures of Si NCs embedded in amorphous SiO_2. B.G.L. and P.S. acknowledge support by the U.S. Department of Energy Solar Energy Technology Program under Contract No. DE-AC36-99GO10337. D.H. and M.Z. acknowledge financial support by DFG (ZA191/27-1 and ZA191/24-1). J.W.L. is supported by the U.S. Department of Energy, Office of Energy Efficiency and Renewable Energy, under Contract No. DE-AC36-08-GO28308. M.C.B and O.E.S. acknowledge support as part of the Center for Advanced Photophysics – an Energy Frontier Research Center funded by the U.S. Department of Energy, Office of Science, Office of Basic Energy Sciences.

Received: February 27, 2012

---

[1] L. T. Canham, *Appl. Phys. Lett.* **1990**, *57*, 1046.
[2] V. Lehmann, U. Gosele, *Appl. Phys. Lett.* **1991**, *58*, 856.
[3] L. Pavesi, L. Dal Negro, C. Mazzoleni, G. Franzo, F. Priolo, *Nature* **2000**, *408*, 440.
[4] S. Tiwari, F. Rana, H. Hana, A. Hartstein, E. F. Crabbe, K. Chan, *Appl. Phys. Lett.* **1996**, *68*, 1377.
[5] G. Conibeer, M. Green, R. Corkish, Y. Cho, E. C. Cho, C. W. Jiang, T. Fangsuwannarak, E. Pink, Y. Huang, T. Puzzer, T. Trupke, B. Richards, A. Shalav, K. Lin, *Thin Solid Films* **2006**, *511*, 654.
[6] M. Jivanescu, A. Stesmans, M. Zacharias, *J. Appl. Phys.* **2008**, *104*, 103518.
[7] S. Cheylan, R. G. Elliman, *Appl. Phys. Lett.* **2001**, *78*, 1225.
[8] M. Zacharias, J. Heitmann, R. Scholz, U. Kahler, M. Schmidt, J. Bläsing, *Appl. Phys. Lett.* **2002**, *80*, 661.
[9] D. Hiller, S. Goetze, F. Munnik, M. Jivanescu, J. W. Gerlach, J. Vogt, E. Pippel, N. Zakharov, A. Stesmans, M. Zacharias, *Phys. Rev. B* **2010**, *82*, 195401.
[10] D. Hiller, M. Jivanescu, A. Stesmans, M. Zacharias, *J. Appl. Phys.* **2010**, *107*, 084309.
[11] A. Stesmans, M. Jivanescu, S. Godefroo, M. Zacharias, *Appl. Phys. Lett.* **2008**, *93*, 023123.
[12] S. Godefroo, M. Hayne, M. Jivanescu, A. Stesmans, M. Zacharias, O. I. Lebedev, G. Van Tendeloo, V. V. Moshchalkov, *Nat. Nanotechnol.* **2008**, *3*, 174.
[13] U. Kahler, H. Hofmeister, *Appl. Phys. A* **2002**, *74*, 13.
[14] A. Irrera, F. Iacona, I. Crupi, C. D. Presti, G. Franzo, C. Bongiorno, D. Sanfilippo, G. Di Stefano, A. Piana, P. G. Fallica, A. Canino, F. Priolo, *Nanotechnology* **2006**, *17*, 1428.
[15] F. Cichos, J. Matin, C. von Borczyskowski, *Phys. Rev. B* **2004**, *70*, 115314.
[16] J. Valenta, A. Fucikova, F. Vácha, F. Adamec, J. Humpolíčková, M. Hof, I. Pelant, K. Kůsová, K. Dohnalová, J. Linnros, *Adv. Funct. Mater.* **2008**, *18*, 2666.
[17] C. Delerue, G. Allan, M. Lannoo, *Phys. Rev. B.* **1993**, *48*, 11024.
[18] W. B. Jackson, N. M. Amer, A. C. Boccara, D. Fournier, *Appl. Opt.* **1981**, *20*, 1333.
[19] A. Zimina, S. Eisebitt, W. Eberhardt, J. Heitmann, M. Zacharias, *Appl. Phys. Lett.* **2006**, *88*, 163103.
[20] J. Tauc, *Amorphous and Liquid Semiconductors* (Plenum, London, **1974**), p. 159.
[21] F. Urbach, *Phys. Rev.* **1953**, *92*, 1324.
[22] A. Podhorodecki, G. Zatryb, J. Misiewicz, J. Wojcik, P. Mascher, *J. Appl. Phys.* **2007**, *102*, 043104.

[23] K. Yoshida, I. Umezu, N. Sakamoto, M. Inada, A. Sugimura, *J. Appl. Phys.* **2002**, *92*, 5936.
[24] P. Mishra, K. P. Jain, *Mat. Sci. Eng. B* **2002**, *95*, 2002.
[25] I. Stenger, L. Siozade, B. Gallas, S. Fisson, G. Vuye, J. Rivory, *Surf. Sci.* **2007**, *601*, 2912.
[26] S. Datta, K. L. Narasimhan, *Phys. Rev. B.* **1999**, *60*, 8246.
[27] B. Garrido, M. López, O. González, A. Pérez-Rodríguez, J. R. Morante, C. Bonafos, *Appl. Phys. Lett.* **2000**, *77*, 3143.
[28] D. Kovalev, H. Heckler, G. Polisski, F. Koch, *Phys. Stat. Sol. (b)* **2002**, *215*, 871.
[29] C. Meier, A. Gondorf, S. Lüttjohann, A. Lorke, H. Wiggers, *J. Appl. Phys.* **2007**, *101*, 103112.
[30] X. J. Hao, E. C. Cho, C. Flynn, Y. S. Shen, G. Conibeer, M. A. Green, *Nanotechnology* **2008**, *19*, 424019.
[31] S. Mirabella, R. Agosta, G. Franzò, I. Crupi, M. Miritello, R. Lo Savio, M. A. Di Stefano, S. Di Marco, F. Simone, A. Terrasi, *J. Appl. Phys.* **2009**, *106*, 103505.
[32] S. Park, E. Cho, D. Song, G. Conibeer, M. A. Green, *Sol. Mat.* **2009**, *93*, 684.
[33] G. Hadjisavvas, P. C. Kelires, *Phys. Rev. Lett.* **2004**, *93*, 226104.
[34] F. Wooten, K. Winer, D. Weaire, *Phys. Rev. Lett.* **1985**, *54*, 1392.
[35] Y. Tu, J. Tersoff, *Phys. Rev. Lett.* **2000**, *84*, 4393.
[36] T. J. Pennycook, G. Hadjisavvas, J. C. Idrobo, P. C. Kelires, S. T. Pantelides, *Phys. Rev. B* **2010**, *82*, 125310.
[37] L. W. Wang, A. Zunger, *J. Chem. Phys.* **1994**, *100*, 2394.
[38] J. W. Luo, A. Franceschetti, A. Zunger, *Nano Lett.* **2009**, *9*, 2648.
[39] L. W. Wang, A. Zunger, *Phys. Rev. B* **1995**, *51*, 17398.
[40] J. W. Luo, P. Stradins, A. Zunger, *Energy Environ. Sci.* **2011**, *4*, 2546.
[41] S. Hernández, A. Martínez, P. Pellegrino, Y. Lebour, B. Garrido, E. Jordana, J. M. Fedeli, *J. Appl. Phys.* **2008**, *104*, 044304.
[42] I. F. Crowe, M. P. Halsall, O. Hulko, A. P. Knights, R. M. Gwilliam, M. Wojdak, A. J. Kenyon, *J. Appl. Phys.* **2011**, *109*, 083534.
[43] A. Stesmans, B. Nouwen, V. V. Afanas'ev, *Phys. Rev. B* **1998**, *58*, 15801.
[44] J. N. Demas, G. A. Crosby, *J. Phys. Chem.* **1971**, *75*, 991–1024.